Proposal for extraction of pore networks with pores of high aspect ratios

Ninghua Zhan [1,2] Rui Wu [1,*] Evangelos Tsotsas [2] and Abdolreza Kharaghani [2]

[1]*School of Mechanical Engineering, Shanghai Jiao Tong University, Shanghai 200240, China*
[2]*Chair of Thermal Process Engineering, Otto von Guericke University Magdeburg,
P.O. 4120, 39106 Magdeburg, Germany*

Pore network modeling is an efficient and reliable approach for simulating the flow and transport of fluids in porous media. A key to this modeling approach is to extract pore networks that can accurately describe the actual pore space of porous media. To extract pore networks from the voxelized porous media, the Euclidean distance map, i.e., the distance of each void voxel to the nearest solid voxel, has been commonly employed so as to discern the hierarchy of the void voxels. However, for the porous media with pores of high aspect ratios, the void voxels can have the same Euclidean distance, and the hierarchy of the void voxels cannot be distinguished clearly by the Euclidean distance map. To address this issue, we propose a pore network extraction method based on the concept of the omnidirectional Euclidean distance, which is a set of Euclidean distances from a void voxel to all the accessible solid boundary voxels. We consider the situation in which two pore bodies are connected by more than one pore throat. Furthermore, a deterministic method is introduced to identify the pore body and the pore throat regions. The proposed pore network extraction method is validated by comparing the pore network modeling results, in terms of the single-phase flow and the quasistatic two-phase drainage, against the direct numerical simulation results and the experimental data. The proposed pore network extraction method not only preserves the topological and morphological properties of the void spaces in porous media, but it is also robust and insensitive to the image noise.

I. INTRODUCTION

The pore network model (PNM) has been widely employed to simulate the pore-scale two-phase transport processes in porous media [1–4]. It has proven to be an efficient approach for simulation of the domains in the order of several representative elementary volumes (REVs) [5,6]. Thus, it can bridge the two-phase interfacial dynamics in the pores of porous media and the transport processes at the continuum scale. In a PNM, the void space of a porous material is extracted as a network composed of large regular pore bodies connected by small regular pore throats. The accuracy of the extracted pore network structures is key to the pore network modeling results. Methods proposed for the extraction of pore networks include the maximal ball (MB) [7–13], watershed segmentation (WS) [14–19], medial axis (MA) [20–25], and generalized pore network extraction [26,27]. In these methods, a porous material of interest is first voxelized; then the Euclidean distance (ED) of each void voxel to the nearest solid voxel is determined. Such an ED map is employed to discern the hierarchy of the void voxels so as to obtain the parameters for the pore network extraction, e.g., the centers of the pore bodies and of the pore throats in the MB methods, the medial axis in the MA algorithm, and the seed voxels for the segmentation of the pore regions in the WS method. However,

---

*Corresponding author: ruiwu@sjtu.edu.cn
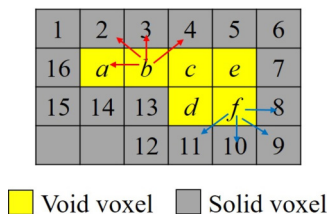
Void voxel ■ Solid voxel

FIG. 1. Schematic of a two-dimensional pore with a high aspect ratio. The solid and void voxels are shown in gray and yellow, respectively. The solid voxels marked with the numbers are the solid boundary voxels. The red arrow indicates the backward direction of voxel b in the first scan. The blue arrow indicates the forward direction of voxel f in the second scan.

for the pores with high aspect ratios, many void voxels can have the same ED. Such pores are very small in some dimensions while very large in others [28]. The hierarchy of the void voxels in a pore of a high aspect ratio cannot be distinguished clearly based on the ED map. For instance, all the void voxels in the pore shown in Fig. 1 have the same ED. The pores of high aspect ratios are commonly encountered in fibrous porous materials, such as the carbon paper gas diffusion layers in proton exchange membrane fuels (PEMFCs) [29]. Development of reliable pore network models for gas diffusion layers will benefit the optimization of water and gas transport in PEMFCs and hence improvements in fuel cell performance.

To accurately extract the pore network structures for porous media with pores of high aspect ratios, we propose an extraction method based on the concept of the omnidirectional Euclidean distance (OED). The OED of a void voxel is a set of EDs from this void voxel to all the accessible solid boundary voxels. A solid boundary voxel has at least one void voxel in its adjacent 8 [two-dimensional (2D)] and/or 26 [three-dimensional (3D)] directions. The line between a void voxel and its accessible solid boundary voxel is not interrupted by any solid voxels. Any two void voxels in a voxelized porous material usually have different OEDs. Hence, the hierarchy of the void voxels can clearly be discerned by using the OED map; see Table I for the OEDs of the void voxels in the pore shown in Fig. 1.

After the hierarchy of void voxels is determined, a pore network mimicking the pore space of a porous material can be extracted through various methods. Among these extraction methods, WS, MB, and MA are the three classical ones. Each extraction methodology has its own advantages and flaws. For instance, MB and WS are praised for the determination of the pore bodies and/or the pore throats. By contrast, MA preserves the topological and morphological properties of the pore space in porous media. To employ the advantages of various extraction methods, different pore network extraction methods have also been combined, e.g., the WS-MB combination [30] and the MA-MB combination [31].

TABLE I. Hierarchical levels and omnidirectional Euclidean distances of the void voxels in the pore shown in Fig. 1.

Hierarchical level	Indexes	Omnidirectional Euclidean distance														
1	a	1	1	1	2	2	2	2	5	8	10	16	17	17	20	0	0
2	b	1	1	2	2	2	4	4	5	5	5	8	9	10	10	13	0
3	f	1	1	2	2	2	4	4	5	5	5	8	9	13	16	17	20
4	d	1	1	2	2	2	4	5	5	5	5	8	10	10	16	17	17
5	e	1	1	2	2	4	4	4	5	5	5	5	8	8	9	10	13
6	c	1	2	2	2	4	4	5	5	5	5	5	5	8	9	10	10

In the MA method [24], a single-voxel-width skeleton is extracted to illustrate the structures of the void space. This skeleton is determined by the thinning algorithm. In the thinning algorithm, the void voxels in the voxelized porous material need to be scanned and checked. A void voxel is marked if it is checked to be inessential, i.e., the so-called simple void voxel [20]. The unmarked or nonsimple void voxels comprise the skeleton of the void space, which is called the medial axis. The extracted medial axis depends on the order of scanning and checking of the void voxels. For this reason, the distance ordered homotopic thinning (DOHT) algorithm has been proposed [32]. In the DOHT algorithm, void voxels are scanned and checked in an increasing ED order, i.e., the void voxel with the smallest ED will be first scanned and checked. The DOHT algorithm, however, fails to detect the pores of high aspect ratios, since the different void voxels can have the same ED (Fig. 1). To overcome this issue, the DOHT algorithm with the symmetric detection has been employed [24]. The extraction results can be improved but are not yet satisfactory.

In the MB method [10], the largest inscribed sphere for each void voxel is determined, and the spheres that are subsets of others are removed. The remaining spheres are the so-called maximal balls, from which the centers of the pore bodies and of the pore throats are determined. Based on these pore centers, the pore body and the pore throat regions are segmented. Two segmentation approaches can be found in the literature. The first is to set the size of the maximal ball at the interface between the pore body and the pore throat regions [10]. For example, a size of 0.7 times the pore body radius is defined artificially in [10]. The second approach is based on the expansion algorithm [31]. In this expansion algorithm, the expansion speed of each region is needed in advance. But, before the pore network extraction, the sizes of pore regions are actually unknown. Thus, the expansion speed cannot be determined accurately and is also defined artificially. The artificial parameters used in these two approaches can result in uncertainty in the pore network extraction.

In the WS method [16], the void space of a porous medium is segmented into a number of pore regions, and the interface between two adjacent pore regions is used to determine the pore throat size. From this point of view, a segmented pore region actually includes a pore body region and part of the connected pore throat regions. The pore body and the pore throat regions are not distinguished.

By addressing the above-mentioned issues and exploiting the advantages of various extraction methods as well as the concept of OED, we propose a feasible way to construct the pore networks that can represent the topological and morphological properties of the void spaces in porous media with pores of high aspect ratios. The method operates as follows:

(i) The OED map is determined so as to obtain the hierarchy of the void voxels.

(ii) The medial axis is extracted based on the hierarchy of the void voxels. To extract the accurate medial axis from a porous medium with pores of high aspect ratios, we propose a thinning algorithm called omnidirectional distance order homotopic thinning (ODOHT). In this algorithm, the void voxels are scanned and checked in increasing OED order. We find that the medial axis determined by the ODOHT algorithm is not only accurate but also insensitive to the image noises, e.g., the noises generated during voxelization of the porous media.

(iii) The centers of the pore bodies and of the pore throats at the medial axis are determined based on the hierarchy of the void voxels, similar to that in the MB method; see [10].

(iv) The pore body and the pore throat regions are segmented by a deterministic method based on the distance of each void voxel to the medial axis.

(v) The pore network is constructed based on the medial axis and the locations of the pore bodies and of the pore throats. To circumvent the issue that two pore bodies are connected by only one pore throat in the previous studies, e.g., [10], the constructed pore network in the present study is composed of nodes connected by bonds. The nodes are the centers of the pore bodies and/or the pore throats. Hence, there are two types of nodes: pore body nodes and pore throat nodes. A bond between two nodes depicts the connection between a pore body and its adjacent pore throat.

The OED-based pore network extraction method proposed in this work has the following distinguished features. First, it can extract pore networks with the topological and morphological

properties of the void spaces from the porous media with pores of high aspect ratios. Second, it is deterministic to identify the pore body and the pore throat regions. Third, it involves the case in which two pore bodies are connected by more than one pore throat. Finally, it is robust and insensitive to the image noise.

In what follows, the concept of the OED is introduced. In Sec. III, the thinning algorithm based on the OED, i.e., the ODOHT algorithm, is presented and validated. In Sec. IV, the centers and regions of the pore bodies and of the pore throats are determined. The procedures to extract the pore network from a porous material is summarized in Sec. V. In Sec. VI, the validation of the simulated single-phase and quasistatic drainage in the pore network extracted from a quasi-2D microfluidic porous medium is performed. Modeling of the single-phase and the quasistatic drainage in the pore network extracted from a 3D fibrous porous material is presented in Sec. VII. Finally, the conclusions are drawn in Sec. VIII.

II. OMNIDIRECTIONAL EUCLIDEAN DISTANCE

The procedures to calculate the OED of each void voxel are introduced in this section. For each void voxel i, $v_{v,i}$, all of its accessible solid boundary voxels are identified. A solid boundary voxel has at least one void voxel in its adjacent 8 (2D) and/or 26 (3D) directions. For instance, as illustrated in Fig. 1, solid voxels 1,2, …,16 are the solid boundary voxels. The line between a void voxel and one of its accessible solid boundary voxels is not interrupted by any solid voxels. A void voxel in a pore of any morphology has at least one accessible solid boundary voxel. The distances between a void voxel i and all of its accessible solid boundary voxels are determined and stored in an array, $OED\_list_{v,i}$, in ascending order. To determine the OED of each void voxel efficiently, the "scan twice" method is employed. The detail procedures are as follows:

(i) Each void voxel i, $v_{v,i}$, is assigned with an array, $ASB\_list_{v,i}$, so as to store the information of the accessible solid boundary voxels. The void voxels are scanned in the forward direction, e.g., from top to bottom and then from left to right, i.e., a-b-c-d-e-f, in Fig. 1. The accessible solid boundary voxels of each scanned void voxel are obtained by checking the neighboring voxels in the backward direction. For instance, the neighboring voxels in the backward direction of voxel b in Fig. 1 are voxels a, 2, 3, and 4. If a neighboring voxel in the backward direction of void voxel i is solid, then this solid voxel is stored as the accessible solid boundary voxel of void voxel i. To this end, after backward direction checking of void voxel a in Fig. 1, we have $ASB\_list_{v,a} =$ [1, 2, 3, 16]. If a neighboring voxel in the backward direction of void voxel i is void voxel j, then the accessible solid boundary voxels of void voxel j are also taken as the accessible solid boundary voxels of void voxel i. As a result, after backward direction checking of void voxel b in Fig. 1, $ASB\_list_b = ASB\_list_a \cup [2, 3, 4] = [1, 2, 3, 16] \cup [2, 3, 4] = [1, 2, 3, 4, 16]$.

(ii) Then the void voxels are scanned in the backward direction, e.g., from bottom to top and then from right to left, i.e., f-e-d-c-b-a in Fig. 1. The accessible solid boundary voxels of each scanned void voxel are obtained by checking the neighboring voxels in the forward direction. For instance, the neighboring voxels in the forward direction of voxel f in Fig. 1 are voxels 8, 9, 10, and 11. The accessible solid boundary voxels of each void voxel are then determined by using the method mentioned in step (i). The accessible solid boundary voxels of each void voxel are the sum of the accessible solid boundary voxels determined in the forward and backward scanning procedures.

(iii) The validity of the accessible solid boundary voxels of each void voxel i is judged by checking whether the line between void voxel i and the accessible solid boundary voxel, e.g., solid boundary voxel j, is interrupted by a solid voxel. If this line is interrupted by a solid voxel, then the accessible solid boundary voxel j is removed from the array $ASB\_list_{v,i}$. For instance, as shown in Fig. 1, the line between solid boundary voxel 14 and void voxel f is blocked by solid voxel 13, thus solid boundary voxel 14 is not an accessible solid boundary voxel of void voxel f.

(iv) The ED between each void voxel i and its accessible solid boundary voxels j is determined as $\sqrt{(x_{v,i} - x_{s,j})^2 + (y_{v,i} - y_{s,j})^2 + (z_{v,i} - z_{s,j})^2}$, for which x, y, and z are the x-, y-, and z-coordinates of voxels, respectively; the subscripts v and s represent the void and solid voxels, respectively. The EDs between each void voxel i and all of its accessible solid boundary voxels are stored in an array $OED\_list_{v,i}$ in increasing order, forming the so-called omnidirectional Euclidean distance (OED). The OEDs of the void voxels in Fig. 1 are listed in Table I. Void voxel i has a larger OED than void voxel j if the first nonzero element in the array $ODE\_list_{v,i} - ODE\_list_{v,j}$ is positive. To this end, the increasing OED order of the void voxels in Fig. 1 is a, b, f, d, e, c. The OED order of the void voxels determines the hierarchy of the void voxels and is defined as the hierarchical level; see the first column in Table I. The larger the OED is, the higher is the hierarchical level. If two void voxels have the same OED, then their hierarchical levels are the same.

III. OMNIDIRECTIONAL DISTANCE ORDER HOMOTOPIC THINNING ALGORITHM

To obtain the medial axis based on the OEDs of the void voxels determined in Sec. II, we propose a modified thinning algorithm, called omnidirectional distance order homotopic thinning (ODOHT). In the ODOHT algorithm, the void voxels of the voxelized porous media are scanned and checked, in increasing OED order, to see if they are the simple ones. Thus, the void voxel with the lowest OED (i.e., the lowest hierarchical level) is scanned and checked first. A void voxel is simple if the topology of the void space is not changed without consideration of this void voxel. The simple void voxels are marked. The scanning and checking are repeated until no new simple void voxel is detected. The skeleton of the void space thus consists of the unmarked void voxels, i.e., the nonsimple ones.

Void voxel i, $v_{v,i}$, in a voxelized porous material is a simple void voxel if the following conditions are satisfied [20,25].

$$G(N_{27}(v_{v,i}) \cap S) = G(N_{26}(v_{v,i}) \cap S), \tag{1}$$

$$O(N_{27}(v_{v,i}) \cap S) = O(N_{26}(v_{v,i}) \cap S) = 1, \tag{2}$$

$$|N_{27}(v_{v,i}) \cap S| > 2 . \tag{3}$$

Here, S is the subset of the unmarked void voxels in the voxelized porous material. $N_{27}(v_{v,i})$ is the structure composed of the void voxel $v_{v,i}$ and its neighboring 26 voxels. $N_{26}(v_{v,i})$ represents the 26 voxels neighboring the void voxel $v_{v,i}$. $N_{27}(v_{v,i}) \cap S$ denotes the unmarked void voxels in $N_{27}(v_{v,i})$. A $3 \times 3 \times 3$ voxel structure with void voxel $v_{v,i}$ at the center is shown in Fig. 2(a). $N_{27}(v_{v,i})$ and $N_{26}(v_{v,i})$ for this structure are illustrated in Figs. 2(b) and 2(c), respectively. $G(\chi)$ is the Euler characteristic of χ. $O(\chi)$ is the number of clusters composed of connected void voxels in χ. χ is the structure of $N_{27}(v_v) \cap S$ or of $N_{26}(v_v) \cap S$. The schematics of $N_{27}(v_v) \cap S$ and of $N_{26}(v_v) \cap S$ are presented in Fig. S1 in the Supplemental Material [33].

The Euler characteristic in Eq. (1) is determined as [20]

$$G(\chi) = v(\chi) - e(\chi) + f(\chi) - o(\chi), \tag{4}$$

where $v(\chi)$, $e(\chi)$, $f(\chi)$, and $o(\chi)$ represent the number of void points, number of void edges, number of void faces, and number of void objects for the structure χ, respectively. For the fast calculation of $G(\chi)$, the structure χ with $3 \times 3 \times 3$ voxels is divided into eight octants, each of which has $2 \times 2 \times 2$ voxels. Figure 2(d) shows one of the eight octants in Fig. 2(b). To this end, we can obtain

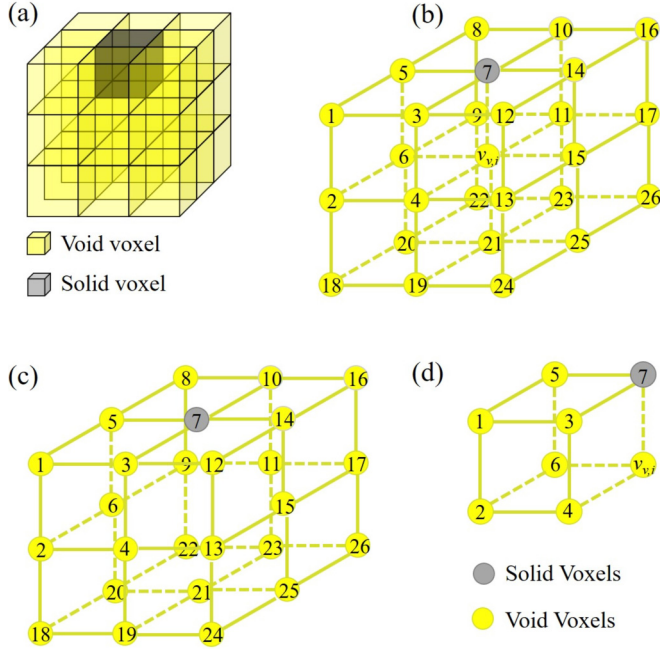$$G(\chi) = \sum_{i=1}^{8} G_{1/8}(\chi_{1/8,i}), \tag{5}$$

FIG. 2. Schematic of (a) a structure of $3 \times 3 \times 3$ voxels, (b) $N_{27}(v_{v,i})$, (c) $N_{26}(v_{v,i})$, and (d) an octant. The solid and void voxels are shown in gray and yellow, respectively. $v_{v,i}$ is the void voxel at the center of the structure shown in (a).

where the subscript 1/8 represents the structure of an octant with $2 \times 2 \times 2$ voxels, i is the octant number, and $G_{1/8}$ is the Euler characteristic of an octant, expressed as [20]

$$G_{1/8}(\chi_{1/8,i}) = \frac{v_{1/8}(\chi_{1/8,i})}{8} - \frac{e_{1/8}(\chi_{1/8,i})}{4} + \frac{f_{1/8}(\chi_{1/8,i})}{2} - o_{1/8}(\chi_{1/8,i}), \qquad (6)$$

where $v_{1/8}$ is the number of void voxels in the octant structure, $e_{1/8}$ is the number of void edges composed of void voxels, $f_{1/8}$ is the number of void faces composed of void voxels, and $o_{1/8}$ is the number of octants composed of void voxels (when all the voxels in the octant are void voxels, $o_{1/8} = 1$, otherwise $o_{1/8} = 0$). The values of $v_{1/8}$, $e_{1/8}$, $f_{1/8}$, and $o_{1/8}$ of the octant shown in Fig. 2(d) with and without consideration of void voxel $v_{v,i}$ are illustrated in Fig. 3. For the octant shown in Fig. 2(d), $o_{1/8} = 0$ since one voxel is the solid voxel. As shown in Fig. 3, if void voxel $v_{v,i}$ is not considered, $v_{1/8}$, $e_{1/8}$, and $f_{1/8}$ are varied from 7 to 6, from 9 to 7, and from 3 to 2, respectively.

Equation (2) is employed to check if the number of void clusters remains unchanged without consideration of a void voxel so as to avoid the breakup of the medial axis during the thinning operation. The number of void clusters is illustrated in Fig. 4. For the structure with $3 \times 3 \times 3$ voxels shown in Fig. 4, there are three void voxels, which are connected to each other. Hence, the number of void clusters is 1. If the central void voxel, $v_{v,i}$, in Fig. 4 is not considered, then the number of void clusters is changed to 2. According to Eq. (2), this central void voxel, $v_{v,i}$, is the nonsimple void voxel.

Equation (3) is used to avoid elimination of the nonsimple void voxels at the inlet and outlet surfaces as well as in the dead pores of the porous material. Figure 5 compares the medial axes of pores extracted with and without Eq. (3). For the sake of clarity, only 2D schematics of the pores and of the extracted medial axes are presented in Fig. 5. The corresponding 3D structures of the pores and of the extracted medial axes are shown in Fig. S2 in the Supplemental Material [33]. In
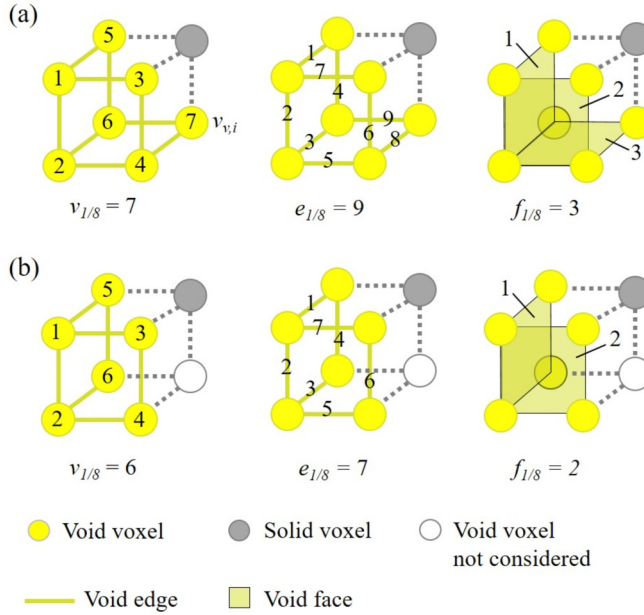
FIG. 3. Values of $v_{1/8}$, $e_{1/8}$, and $f_{1/8}$ for the octant shown in Fig. 2(d) (a) with and (b) without consideration of the void voxel $v_{v,i}$. The void voxel, solid voxel, and void voxel not considered are shown in yellow, gray, and white, respectively. The line between two void voxels is the void edge. The face formed by four void voxels is the void face. $v_{1/8}$ is the number of void voxels in the octant structure. $e_{1/8}$ is the number of void edges composed of void voxels. $f_{1/8}$ is the number of void faces composed of void voxels. $o_{1/8}$ is the number of octants composed of void voxels (when all the voxels in the octant are void voxels, $o_{1/8} = 1$, otherwise $o_{1/8} = 0$). The void voxels, void edges, and void faces are numbered in this figure.

Fig. 5(a), a straight pore is considered; see the left image. The extracted medial axis is a straight line if Eq. (3) is considered; see the middle image. If Eq. (3) is not considered, then the extracted medial axis is just a point; see the right image. Intuitively, the medial axis of a straight tube shall be a straight line. Thus, Eq. (3) needs to be considered so as to obtain the reasonable medial axis. It should be noted that the medial axis in the middle image of Fig. 5(a) is not as long as the pore length. The reason is that the nonsimple void voxels at the inlet and outlet surfaces are not identified first. Determination of the nonsimple void voxels at the inlet and outlet surfaces is illustrated in detail in the following paragraphs.

In Fig. 5(b), a straight pore with a branch is considered. In this case, the nonsimple void voxels at the inlet and outlet surfaces are determined first; see the left image. The medial axes extracted with and without Eq. (3) are presented in the middle and the right images, respectively. The medial axis of the main straight tube can be obtained even though Eq. (3) is not considered. But, the medial axis of the branch is obtained only when Eq. (3) is taken into account. Thus, Eq. (3) should be considered so as to extract the reasonable medial axis.

Compared to the internal void voxels, the void voxels at the inlet and the outlet surfaces are connected to the environment. Hence, the simple void voxels at these two surfaces should be identified independently (the other surfaces are covered by the solid voxels). On the other hand, determination of the simple void voxels inside the porous material near the inlet or the outlet surface depends on the state (simple or not) of the void voxels at these two surfaces. As a result, the simple void voxels at the inlet and outlet surface should be identified first.

The simple void voxels at the inlet and outlet surfaces of a voxelized porous material are determined as follows (also illustrated in Fig. S3 in the Supplemental Material [33]). First, the
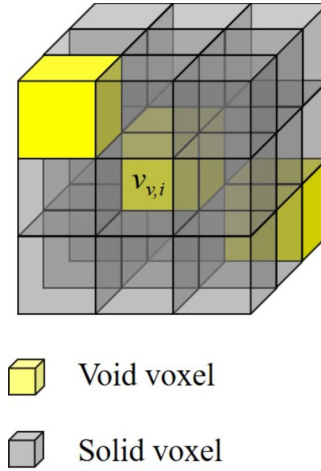
FIG. 4. Schematic of a structure of $3 \times 3 \times 3$ voxels with one void cluster composed of three connected void voxels. If the central void voxel, $v_{v,i}$, is not considered, then the number of void clusters increases to 2.

void clusters (2D) at each surface are determined. A void cluster is the one composed of only void voxels connected to each other. As illustrated in Fig. S3b, there are seven void clusters. Then the OED of each void voxel at the surface is calculated; here, the Euclidean distance is 2D, i.e., from a void voxel to an accessible solid boundary voxel in the same surface. Based on the OED map, the hierarchical levels of the void voxels are determined; see Fig. S3c. In each void cluster, the void voxel with the highest hierarchical level is identified and set as the nonsimple one, and the other void voxels are set as the simple ones; see Fig. S3d.

The nonsimple void voxels at the inlet and outlet surfaces are marked as anchors and retained during the subsequent thinning operations applied to internal void voxels, as illustrated in the left two images in Fig. 5(b). If the nonsimple void voxels at the inlet and outlet surfaces are not determined first, then the extracted medial axis is not complete; see the left two images in Fig. 5(a).
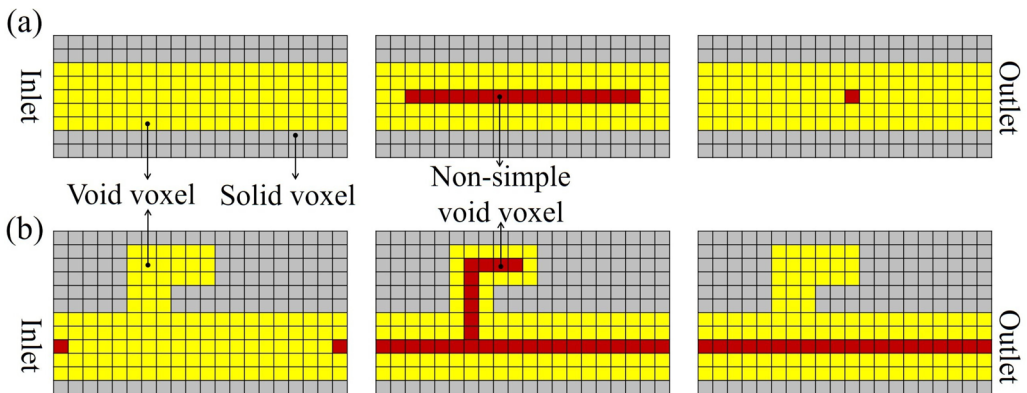

FIG. 5. 2D schematics of the extracted medial axes in pores. (a) Extraction of the medial axis from a straight pore: left, structure of the straight pore; middle, medial axis extracted with Eq. (3); right, medial axis extracted without Eq. (3). (b) Extraction of the medial axis from a straight pore with a branch: left, structure of the pore with the nonsimple void voxels at the inlet and outlet surfaces; middle, medial axis extracted with Eq. (3); right, medial axis extracted without Eq. (3). The corresponding 3D structures of the pores and of the extracted medial axes are shown in Fig. S2 in the Supplemental Material [33].
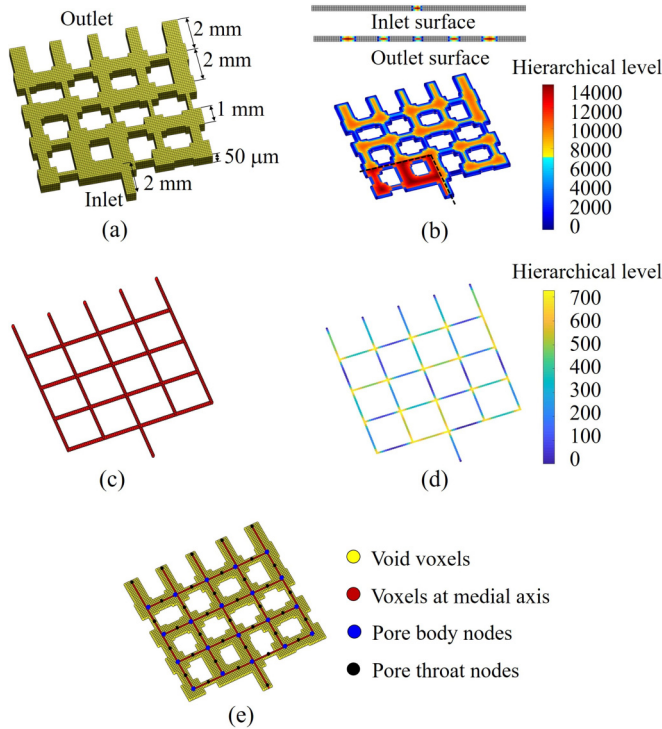
FIG. 6. Extraction of the pore network from (a) a void space of a microfluidic pore network. (b) The hierarchical level of void voxels in the void space. (c) The extracted medial axis. (d) The hierarchical level of the void voxels at the medial axis. (e) The extracted pore network with the pore body and the pore throat nodes.

After the thinning operations are finished, these nonsimple void voxels at the inlet and outlet surfaces are set as the nodes at the medial axis of the voxelized porous material.

To validate the proposed ODOHT algorithm, it is employed to extract the medial axis of a quasi-2D microfluidic pore network composed of pores with the same thickness of 50 μm. The pore bodies are square and with a side length of 1 mm in the plane perpendicular to the thickness direction. The distance between the centers of two neighboring pore bodies is 2 mm [Fig. 6(a)]. The pore throat widths are varied from 100 to 940 μm. Hence, these pores have a high aspect ratio. The width of each pore throat is presented in Fig. S4 in the Supplemental Material [33]. The hierarchical levels of the void voxels and the medial axis for the microfluidic pore network obtained based on the ODOHT algorithm are presented in Figs. 6(b) and 6(c). The relevant results obtained by the traditional DOHT algorithm based on the ED map are shown in Fig. S5 in the Supplemental Material [33].

As shown in Fig. S5a in the Supplemental Material [33], the largest hierarchical level of the void voxel determined based on ED is 4. Thus, many void voxels have the same ED. The hierarchical level is employed to determine the scanning order in the thinning algorithm. The void voxel with the lowest hierarchical level will be scanned and checked first. The void voxels with the same (omnidirectional) ED are in the same hierarchical level. The scanning order of these void voxels with the same hierarchical level is randomly determined in the ED-based DOHT algorithm. When many void voxels have the same hierarchical level, the scanning order shall be rather random, thereby deteriorating the extraction of the medial axis.

By contrast, the largest hierarchical level of the void voxel determined based on OED can reach 14 000; see Fig. 6(b). Hence, the scanning order of the void voxels is more deterministic in the OED-based ODOHT algorithm than in the ED-based DOHT algorithm. It should be noted that
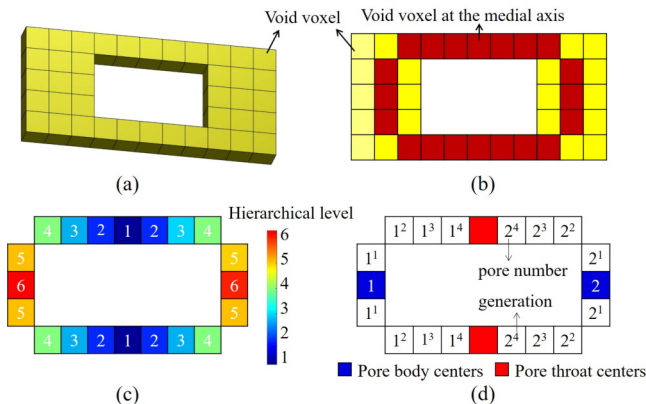
FIG. 7. (a) Determination of the centers of pore bodies and pore throats in a void structure. (b) The extracted medial axis. (c) The hierarchical level of the void voxels at the medial axis. (d) The determined centers of the pore bodies and of the pore throats.

the void voxels can also have the same hierarchical level in the ODOHT algorithm [e.g., see the hierarchical level shown in Fig. 7(c)]. But, since the OED is employed to determine the hierarchical level, only the spatially symmetric void voxels can have the same hierarchical level. The scanning order of the spatially symmetric void voxels, on the other hand, will not influence the extraction results. As a result, the media axis obtained by the ODOHT algorithm is smoother and more desirable than the one obtained by the traditional DOHT algorithm. We also find that the medial axis extracted by the ODOHT algorithm can be insensitive to the image noise, as elucidated in Appendix A.

IV. LOCATIONS OF PORE BODIES AND PORE THROATS

A. Centers of pore bodies and pore throats

Based on the medial axis extracted by the ODOHT algorithm, the centers of the pore bodies and of the pore throats can be determined by using the following algorithms. Take the void structure shown in Fig. 7(a) as an example. Initially, $PB(v_{v,ma,i}) = 0$ is applied to each void voxel i at the medial axis, $v_{v,ma,i}$, and the pore body number is $N_{pb} = 0$. $PB(v_{v,ma,i})$ denotes the pore body to which void voxel i is associated. The medial axis for the void structure in Fig. 7(a) is shown in Fig. 7(b). Then, the void voxels at the medial axis are scanned and checked in descending OED order; see Fig. 7(c). The highest hierarchical level is 6. The following rules are applied to each scanned void voxel in the medial axis:

(1) If a scanned void voxel i, $v_{v,ma,i}$, has $PB(v_{v,ma,i}) = 0$, then this void voxel is the ancestor void voxel and is the center of a pore body; see the blue points in Fig. 7(d). This indicates that a new pore body is generated. Thus, the pore body number, N_{pb}, is updated as $N_{pb} = N_{pb} + 1$; then, the pore body to which void voxel i is associated is $PB(v_{v,ma,i}) = N_{pb}$. After this, each void voxel j in the medial axis with a smaller OED adjacent to void voxel i is scanned.

(1.1) If $PB(v_{v,ma,j}) = 0$, then void voxel j has not been associated with any pore body. Thus, void voxel j is the first generation of the ancestor void voxel associated with the pore body N_{pb}, and $PB(v_{v,ma,j}) = PB(v_{v,ma,i})$; see the void voxels 1^1 and 2^1 in Fig. 6(d) (the superscript 1 represents the first generation).

(1.2) If $PB(v_{v,ma,j}) > 0$, then void voxel j is already associated with a pore body. This indicates that void voxel j is associated with two pore bodies. In this regard, $v_{v,ma,j}$ is the center of a pore throat; see the red points in Fig. 7(d).

(2) If a scanned void voxel i, $v_{v,\mathrm{ma},i}$, has $\mathrm{Pore}(v_{v,\mathrm{ma},i}) > 0$, then check each adjacent void voxel j in the medial axis with a smaller OED.

(2.1) If $\mathrm{Pore}(v_{v,\mathrm{ma},j}) = 0$, then $\mathrm{Pore}(v_{v,\mathrm{ma},j}) = \mathrm{Pore}(v_{v,\mathrm{ma},i})$, and if the pore number of void voxel i is the nth generation of an ancestor void voxel, then the pore number of void voxel j is the $(n + 1)$th generation.

(2.2) If $\mathrm{Pore}(v_{v,\mathrm{ma},j}) > 0$, then void voxel j is already associated with a pore body. This means that void voxel j is the center of a pore throat.

Based on the above rule, the centers of the pore bodies and of the pore throats at the medial axis can be determined; e.g., see Fig. 7. As illustrated in Fig. 7(d), the two pore bodies are connected by more than one pore throat. The determined centers of the pore bodies and of the pore throats at the medial axis of the microfluidic pore network shown in Fig. 6(a) are also illustrated in Figs. 6(d) and 6(e). As can be seen, the determined centers are accurate.

B. Regions of pore bodies and pore throats

Once the centers of the pore bodies and the pore throats are obtained, the regions of the pore bodies and the pore throats can then be determined by using the following algorithm (also illustrated in Fig. 8):

(i) The medial axis is divided into a number of unit axes, each of which is connected to two pore body centers; see Fig. 8(a). For each void voxel i, $v_{v,i}$, $\mathrm{axis}(v_{v,i}) = 0$ is applied. $\mathrm{axis}(v_{v,i})$ represents the unit axis nearest to $v_{v,i}$. The unit axes for the medial axis of the microfluidic pore network shown in Fig. 6(a) are presented in Fig. S6a in the Supplemental Material.

(ii) For each void voxel i, $v_{v,i}$, its nearest unit axis, e.g., unit axis t, is determined, and then $\mathrm{axis}(v_{v,i}) = t$. As shown in Fig. 8(a), the unit axis nearest to $v_{v,i}$ is unit axis 4; thus, $\mathrm{axis}(v_{v,i}) = 4$. If a void voxel has two nearest unit axes, then this void voxel is marked as the common void voxel; its nearest unit axis number is set as 0; see the yellow void voxels shown in Fig. 8(b). The void voxels in the microfluidic pore network shown in Fig. 6(a) with the same nearest unit axis are illustrated in Fig. S6b in the Supplemental Material.

(iii) The cross-sectional plane perpendicular to each void voxel at the medial axis, e.g., $v_{v,\mathrm{ma},i}$, is determined. The cross-sectional plane passes through void voxel $v_{v,\mathrm{ma},i}$, and it is perpendicular to the line between the two void voxels at the medial axis adjacent to $v_{v,\mathrm{ma},i}$. For the void voxels touched by the same cross-sectional plane, if these void voxels have the same nearest axis, then they are in a pore throat region; see the cross-sectional plane 1 in Fig. 8(b); if these void voxels have different nearest unit axes, then they are in a pore body region; see the cross-sectional plane 2 in Fig. 8(b).

(iv) The void voxels not touched by the cross-sectional plane are scanned iteratively with the following rule to determine whether they are in the pore body or in the pore throat regions. A nontouched void voxel is in a pore throat region if it is connected to only the void voxels in the pore throat regions. A nontouched void voxel is in a pore body region as long as it is connected to a void voxel in a pore body region.

The segmented pore body and pore throat regions for the void space of the microfluidic pore network shown in Fig. 6(a) can be found in Fig. S6c in the Supplemental Material. Clearly, the determined pore body and pore throat regions are in accordance with the structures of the microfluidic pore network shown in Fig. 6(a).

V. PROCEDURE TO EXTRACT THE PORE NETWORK FROM A POROUS MATERIAL

The pore network of a porous material can be extracted by using the following procedures:

(i) Identify the nonsimple void voxels at inlet and outlet surfaces based on the idea detailed in Sec. III.

(ii) Determine the media axis of the voxelized porous material based on the ODOHT algorithm detailed in Sec. III.
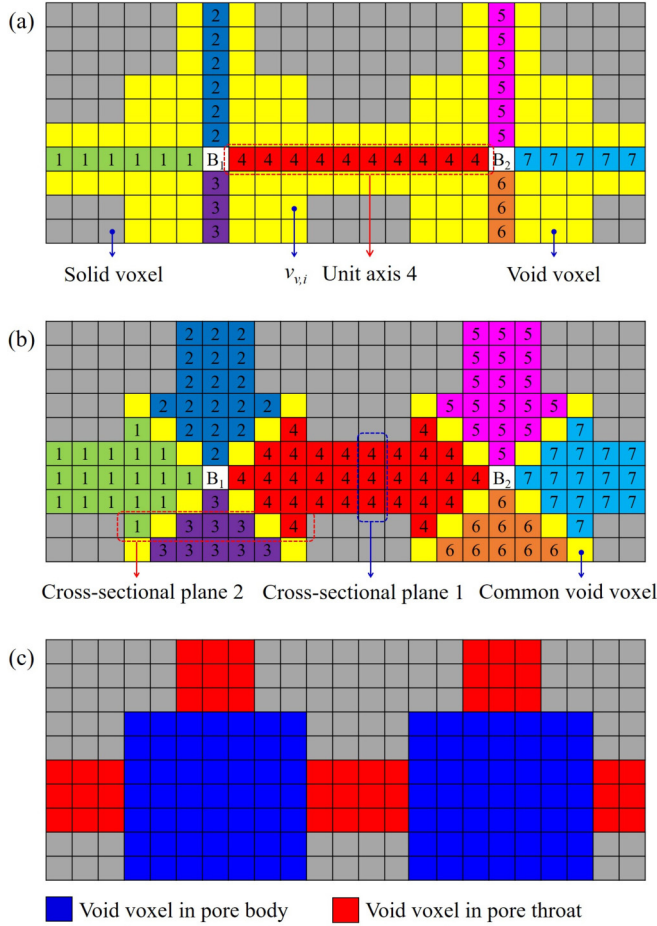
FIG. 8. Procedures to determine the pore body and the pore throat regions. (a) The unit axes in the medial axis are determined. The void voxels with the numbers are the unit axis, e.g., unit axis 4. (b) The nearest unit axis for each void voxel is determined. If a void voxel has two nearest unit axes, then it is set as the common void voxel; see the yellow void voxels. (c) The pore body and the pore throat regions are determined. If all the void voxels in the cross-sectional plane perpendicular to the medial axis have the same nearest unit axis, then these void voxels are in the pore throat regions; see cross-sectional plane 1 in (b). If the void voxels in the cross-sectional plane perpendicular to the medial axis have a different nearest unit axis, then these void voxels are in the pore body regions; see cross-sectional plane 2 in (b).

(iii) Determine the locations, i.e., centers and regions, of the pore bodies and the pore throats; see Sec. IV.

(iv) Construct the pore network based on the media axis and the locations of the pore bodies and the pore throats. In previous pore network extraction methods, two pore bodies are usually connected by only one pore throat. But in reality, two pore bodies can be connected by more than one pore throat; see Fig. 7. To address this issue, both the centers of the pore bodies and of the pore throats are considered as the centers of the nodes in the extracted pore network. As a result, the extracted pore network is composed of nodes connected by bonds. The centers of nodes are the centers of the pore bodies or the pore throats. A bond between two nodes represents the connection between a pore body and its neighboring pore throat. Thus, there are two types of nodes: pore body nodes and pore throat nodes, as illustrated in Fig. 6(e).

The pore network extracted from the void space of the microfluidic pore network shown in Fig. 6(a) is presented in Fig. 6(e). The extracted pore network preserves well the structure of the void space. The medial axes and the pore networks extracted based on the traditional ED map are also presented in Fig. S5 in the Supplemental Material [33] for comparison. Comparison of Fig. 5 and Fig. S5 indicates that the extracted medial axis and pore network based on the OED map are more desirable than those obtained based on the traditional ED map.

For the OED-based pore network extraction method, all the accessible solid boundary voxels of each void voxel need to be determined. By contrast, only the nearest solid boundary voxel of each void voxel needs to be identified in the ED-based method. Hence, it takes a longer time to determine the hierarchical levels of void voxels for the OED-based method than for the ED-based method. The computational time to obtain the hierarchical level for the microfluidic pore network shown in Fig. 6(a) is 22.39 s for the OED-based method and 4.34 s for the ED-based method. The computational time to extract the pore network based on the hierarchical levels of void voxels is 9.31 s for the OED-based method and 8.33 s for the OED-based method. Hence, as compared to the ED-based pore network extraction method, the OED-based method proposed in the present study is more accurate to extract the medial axis and the pore network, but it also requires more computational resources.

VI. VALIDATION OF THE SINGLE-PHASE FLOW AND THE QUASISTATIC DRAINAGE IN THE PORE NETWORK EXTRACTED FROM A QUASI-2D POROUS MATERIAL

To validate the effectiveness of the extracted pore network, we compare the pore network modeling results against the direct numerical simulation results as well as the experimental data in terms of the single-phase flow and the quasistatic drainage of a nonwetting phase displacing a wetting phase in the microfluidic pore network shown in Fig. 6(a).

A. Single-phase flow

For the single-phase flow in the pore network, the pressure field can be obtained by applying the mass conversation law to each node i:

$$\sum_{j=1}^{n_i} g_{ij}\mu(P_j - P_i) = 0, \tag{7}$$

where μ is the dynamic viscosity of fluid, g_{ij} is the flow conductivity between nodes i and j, and n_i is the number of nodes adjacent to node i. To determine g_{ij}, the void space between nodes i and j is divided into a series of slices along the media axis between these two nodes. Each slice has a single-voxel thickness and is perpendicular to the media axis. To this end, we have

$$\frac{1}{g_{ij}} = \sum \frac{1}{g_{s,m}}, \tag{8}$$

where $g_{s,m}$ represents the flow conductivity of the mth slice. Since the pores in the model porous material shown in Fig. 5(a) are cuboid, the slices for calculating g_{ij} have a rectangular cross section, and $g_{s,m}$ is determined as

$$g_{s,m} = \frac{2A_{s,m}k_{s,m}}{l_{s,m}}, \tag{9}$$

where $A_{s,m}$ and $l_{s,m}$ are the cross-sectional area and length of the mth slice, respectively; $k_{s,m}$ is

$$k_{s,m} = \frac{2}{Po_{s,m}}\left[\frac{w_{s,m}h_{s,m}}{w_{s,m} + h_{s,m}}\right]^2, \tag{10}$$

where $w_{s,m}$ and $h_{s,m}$ are the width and height of the cross section of the mth slice; $\mathrm{Po}_{s,m}$ is the Poiseuille number, and it is expressed as [34]

$$\mathrm{Po}_{s,m} = 14.277 + 1402.5\left[\frac{1 + \frac{w_{s,m}}{h_{s,m}}(\sqrt{2}-1)}{4\left(1 + \frac{w_{s,m}}{h_{s,m}}\right)} - \frac{\sqrt{2}}{8}\right]^2. \tag{11}$$

After g_{ij} is determined, the pressure field in the extracted pore network can be obtained by solving the linear equations established based on Eq. (7) and the boundary conditions. The air flow in the microfluidic pore network shown in Fig. 6(a) is simulated. The air flow rate is 10^{-5} kg/s at the inlet, and the pressure is zero at the outlet. The pore network model shows that the inlet pressure is 268.88 Pa. This value is similar to 275.6 Pa obtained from direct numerical simulation based on the software COMSOL. The relative error of the pore network modeling inlet pressure is 2.44% (the computational time is 0.072 s).

The inlet pressures predicted by the ED-based pore network model are also presented in Fig. S7 in the Supplemental Material [33] for comparison. For the ED-based pore network model, the flow conductivity between a pore throat node and a pore body node is determined based on the distance between them and the radius of the pore throat, same as that in [16]. The relative error of the inlet pressure determined by the ED-based pore network model is 25.8% (the computational time is 0.033 s). If the cross section of the pore throat and the distance between two nodes are used to determine flow conductivity between these two nodes, similar to Eq. (9), then the relative error of the inlet pressure determined by the ED-based pore network model is 17% (the computational time is 0.069 s). The inlet pressure predicted by the OED-based pore network model is more accurate than that predicted by the ED-based pore network model. The computational time to solve the single-phase flow in the extracted pore network is higher for the OED-based pore network model than for the ED-based pore network model.

B. Quasistatic drainage

For the quasistatic drainage of a nonwetting phase displacing a wetting phase in a porous material, the nonwetting phase invades a pore occupied by the wetting phase only if the difference in the pressure between the nonwetting and the wetting phases is equal to or larger than the threshold pressure of the pore. Hence, to simulate the quasistatic drainage in the extracted pore network composed of nodes connected by bonds, it is necessary to determine the threshold pressure of each node.

The threshold pressure of a pore depends on the pore morphology and wettability, e.g., the capillary valve effect induced by the sudden geometrical expansion and the corner films due to the residual wetting phase at the pore corners. These two effects, however, are not considered in the present study. To this end, the threshold pressure of node i for the drainage from nodes j to i or from nodes i to j is determined as follows. The slice with a single-voxel thickness at the center of node i and perpendicular to the medial axis between nodes i and j is identified. For the quasistatic two-phase displacement, the work needed to push the nonwetting phase to occupy the single-voxel-thick slice is equal to the change of the surface energy:

$$\Delta P A_{s,m} dh_{s,m} = \sigma_{nw-w} dS_{s,m,nw-w} + \sigma_{s-nw} dS_{s,m,s-nw} + \sigma_{s-w} dS_{s,m,s-w}, \tag{12}$$

where $\Delta P = P_{nw} - P_w$ is the pressure difference between the nonwetting and the wetting phases, $A_{s,m}$ is the cross-sectional area of the mth slice, $dh_{s,m}$ is the infinitesimal distance along the thickness direction of the slice, σ is the surface tension, and $S_{s,m}$ is the interfacial area in the mth slice. The subscripts nw, w, and s are the nonwetting phase, the wetting phase, and the solid, respectively.

During the quasistatic invasion of the nonwetting phase into the slice initially occupied by the wetting phase, the shape of the interface between the nonwetting and wetting phases is assumed to remain unchanged, and hence $dS_{s,m,nw-w} = 0$. By contrast, $dS_{s,m,s-nw}$ and $dS_{s,m,s-w}$ can be

expressed as

$$dS_{\text{s},ms\text{-nw}} = C_{\text{s},m}dh_{\text{s},m}, \quad dS_{\text{s},m,\text{s-w}} = -C_{\text{s},m}dh_{\text{s},m}, \tag{13}$$

where $C_{\text{s},m}$ is the perimeter of the cross section of the mth slice. On the other hand, the surface tensions are correlated:

$$\sigma_{\text{s-nw}} - \sigma_{\text{s-w}} = \sigma_{\text{nw-w}}\cos\theta_e, \tag{14}$$

where θ_e is the equilibrium contact angle taken in the wetting phase. For quasistatic two-phase displacement in a pore, it is reasonable to assume that the contact angle is equal to θ_e. Based on Eqs. (12)–(14), we can obtain

$$\Delta P = \sigma_{\text{nw-w}}\cos\theta_e\frac{C_{\text{s},m}}{A_{\text{s},m}}. \tag{15}$$

Equation (15) indicates that in order to make the invasion of the nonwetting phase into the mth slice happen, the difference in pressure between the nonwetting and the wetting phases should be equal to or larger than $\sigma_{\text{nw-w}}\cos\theta_e C_{\text{s},m}/A_{\text{s},m}$, which is the so-called threshold pressure.

The following algorithm is employed to simulate the quasistatic drainage in the extracted pore network composed of the nodes and the bonds.

(i) The available nodes are identified. A node is available if it is occupied by the wetting phase, adjacent to at least one node occupied by the nonwetting phase, and connected to the outlet through the wetting phase paths.

(ii) The entry pressure for the nonwetting phase to invade the available node is determined. For the nonwetting phase invading an available node, e.g., node i from the adjacent node j, the nonwetting phase needs to move out of node j and enter into node i. To accomplish this process, the difference between the nonwetting and the wetting phases should be equal to or larger than $\max(P_{t,j\to i}, P_{t,i\gets j})$, for which $P_{t,j\to i}$ and $P_{t,i\gets j}$ are the threshold pressures for nodes j and i along the media axis between nodes i and j, respectively. Hence, the entry pressure is $\max(P_{t,j\to i}, P_{t,i\gets j})$.

(iii) The available node with the lowest entry pressure is identified and is invaded by the nonwetting phase.

(iv) The phase distribution in the pore network is updated. The trapped nodes, occupied by the wetting phase and surrounded by the nodes filled with the nonwetting phase, are identified. The invasion into the trapped nodes and bonds is excluded.

(v) Repeat steps (i)–(iv) until the prescribed condition is satisfied.

The quasistatic drainage in the extracted pore network is simulated by using the above algorithm. The simulation results regarding the variations of the phase distribution and the saturation and the number of the gas (wetting phase) clusters during the quasistatic drainage are compared against the experimental data; see Fig. 9 and Fig. S8 in the Supplemental Material [33]. In the experiment, water is the invading fluid (the nonwetting phase) and air is the displaced fluid (the wetting phase); the microfluidic pore network is fabricated based on Polydimethylsiloxane (PDMS). The pore sizes of the microfluidic pore network shown in Fig. 6(a) are detailed in Fig. S3. The microfluidic pore network is initially filled with the wetting phase, i.e., air. The nonwetting phase, water, is then injected into the inlet of the pore network, with a flow rate of 0.1 μL/min. For such a low flow rate, the capillary number is about 10^{-8}, and the two-phase flow is a quasistatic process and thus controlled by the capillary forces. Detailed information on the experiment can be found in [35].

Overall, the OED-based pore network modeling results have a good agreement with the experimental data. In particular, the predicted pore bodies invaded by the nonwetting phase are the same as the experimental results. On the other hand, the pore network model indicates fewer pore throats occupied by the nonwetting phase (water). The main reason is that the capillary valve effect induced by the sudden geometrical expansion is not considered in the present pore network study. A detailed explanation of the capillary valve effect can be found in [35], as well as the reasons
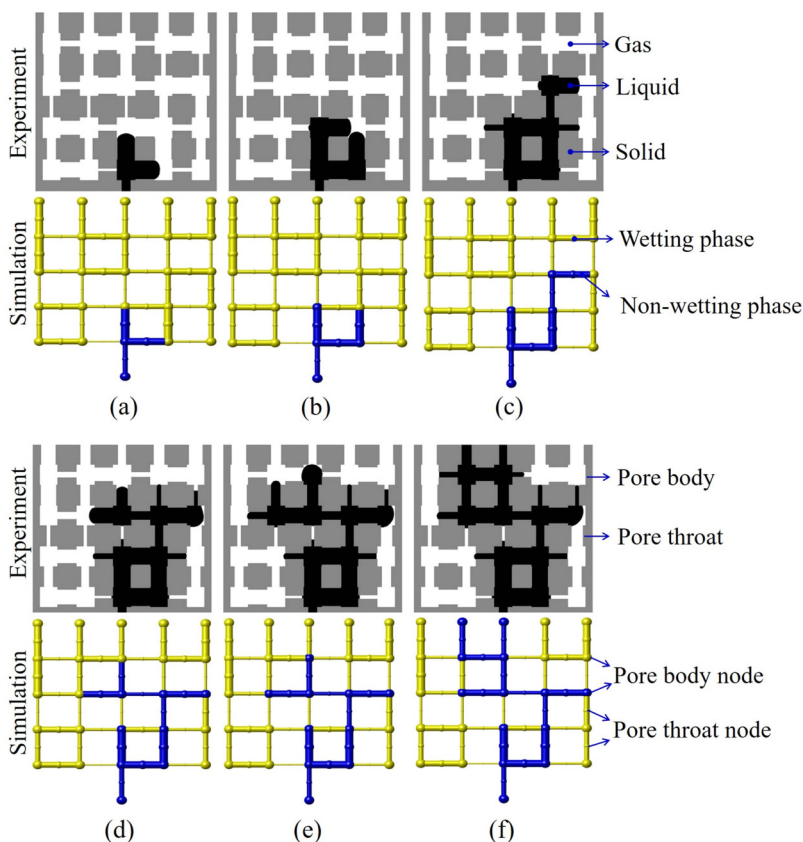
FIG. 9. Comparison of the pore network modeling and the experimental results for the phase distribution at various stages (a)–(f) during the quasistatic drainage in the microfluidic pore network shown in Fig. 6(a). In the experimental results, the solid (PDMS), liquid (nonwetting phase), and gas (wetting phase) are shown in gray, black, and white, respectively. In the simulation results, the nonwetting phase and the wetting phase filled pores are shown in blue and yellow, respectively.

for the difference between the simulation results for the cases with and without the capillary valve effect.

The variations of the phase distribution obtained by the ED-based pore network models are also presented in Fig. S9 in the Supplemental Material [33] for comparison. In the ED-based pore network model, two approaches are employed to calculate the threshold pressure. In the first method, the threshold pressure of a pore is determined as $2\sigma_{\text{nw-w}}/r_{p,\text{ED}}$, for which $r_{p,\text{ED}}$ is the ED of the pore center. The second approach is the one used in the present study, i.e., Eq. (15). No matter which approach is employed to determine the threshold pressure, the variation of the phase distribution obtained by the ED-based pore network model deviates from the experimental data.

As illustrated in Fig. 9 and Fig. S9 in the Supplemental Material [33], the variation of the phase distribution during quasistatic drainage predicted by the OED-based pore network model is more accurate than that simulated by the ED-based pore network model. The computational time to simulate the quasistatic drainage process in the extracted pore network is higher for the OED-based pore network model (0.209 s) compared to the ED-based pore network model (0.046 s for the first method to determine the threshold pressure and 0.091 s for the second method).
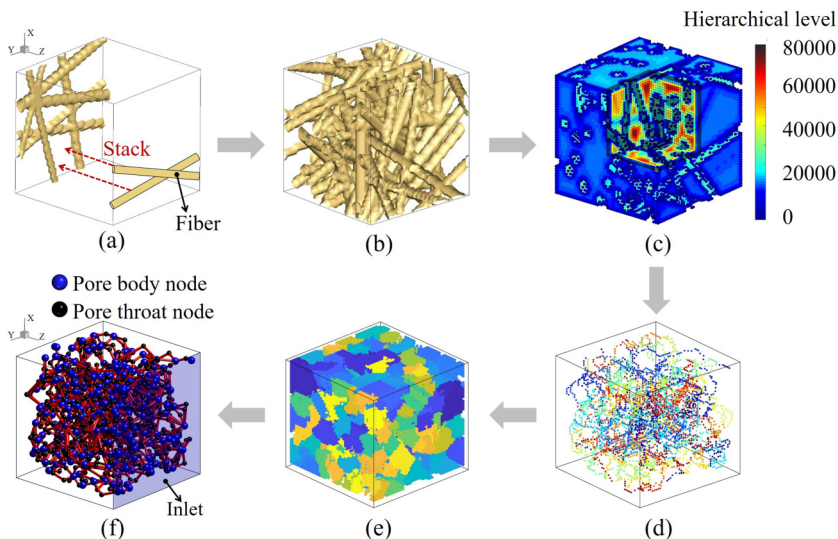
FIG. 10. Procedures to extract the pore network from a fibrous porous material generated numerically. (a) Schematic of the numerical generation of a fibrous porous material based on the stacking of the cylindrical fibers. The radius of each cylindrical fiber is 3.5 μm. (b) 3D view of the generated fibrous porous material with the size of 50 μm × 50 μm × 50 μm. (c) The OED-based hierarchical levels of the void voxels, (d) extracted medial axis, (e) pore throat and pore body regions, and (f) extracted pore network of the voxelized fibrous porous material with 50 voxels in each direction.

VII. SINGLE-PHASE FLOW AND QUASISTATIC DRAINAGE IN THE PORE NETWORK EXTRACTED FROM A 3D FIBROUS POROUS MATERIAL

To further demonstrate the feasibility of the pore network extraction algorithm proposed above, we present in this section the pore network extracted from a 3D fibrous porous material. The single-phase flow and the quasistatic drainage in the extracted pore network are also simulated. The 3D fibrous porous material is numerically constructed. The straight cylindrical fibers with the same radius of 3.5 μm are randomly stacked layer by layer on a base surface. Each layer has a thickness of 7 μm and a porosity of about 0.75. All the cylindrical fibers are parallel to the base surface, as illustrated in Fig. 10(a). The constructed 3D fibrous porous material, as shown in Fig. 10(b), has a size of 50 μm × 50 μm × 50 μm. It is voxelized to have 50 voxels in each direction for the pore network extraction. Each voxel is cubic with a side length of 1 μm.

A. Pore network extraction

The OED-based hierarchical levels of the void voxels in the fibrous porous material are illustrated in Fig. 10(c). The ED-based hierarchical levels are presented in Fig. S10 in the Supplemental Material [33] for comparison. As shown in Fig. S10, most of the void voxels have the same hierarchical level. By contrast, the hierarchy of the void voxels in the voxelized fibrous porous media can be distinguished clearly based on OED; see Fig. 10(c).

Based on the hierarchical level of the void voxel shown in Fig. 10(c), the medial axis, pore throat and pore body regions, and the extracted pore network composed of nodes and bonds can be obtained; see Figs. 10(d)–10(f). The number of pore throats and pore bodies is 894 and 367, respectively. The extracted pore network represents essentially the morphology of the void space in the fibrous porous material. It should be noted that the spherical nodes and cylindrical bonds in the extracted pore network shown in Fig. 10(f) are just a schematic and not the real shapes. We find that for the fibrous porous material shown in Fig. 10(b), the pore throat regions can be thin along the
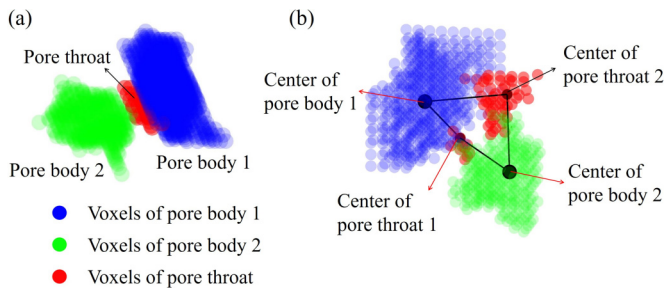
FIG. 11. Examples of pore throat and pore body regions in the fibrous porous material shown in Fig. 10. (a) The pore throat region is thin along the medial axis. (b) Two pore body regions can be connected by more than one pore throat region.

medial axis; see Fig. 11(a). Two pore body regions can be connected by more than one pore throat; see Fig. 11(b). In addition, some pore throat regions contain only one void voxel. This could be due to the fact that the resolution of the voxelized fibrous porous material is not enough to capture the detailed structures of the small pores.

Note that the centers of two pore body regions can be close, e.g., only 2 voxels distance; see Fig. S11 in the Supplemental Material [33]. Merging of two or more pore body regions close to each other is not considered in our extraction algorithm. The reason is that the pore throats between two adjacent pore body regions can be small; see the average radii of the pore bodies and of the pore throats in Fig. S12 in the Supplemental Material [33]. The average pore radius is defined in Eq. (16). In the drainage processes, once a pore body region is invaded by the nonwetting fluid, its invasion into the adjacent pore body region can be hindered by the small pore throats between the pore body regions. To model accurately the drainage processes in the extracted pore network, the merging of the adjacent pore body regions is not considered, even though such a merge can reduce the complexity of the extracted pore network. The detailed distributions of the sizes of pore bodies and of pore throats as well as the pore connectivity are presented in the following paragraphs.

Since the pores have high aspect ratios, the pore sizes are different in different directions. In this way, we defined the average radius of a pore as the averaged value of the distances from the pore center voxel to all the accessible voxels that wrap the pore region:

$$r_{p,\mathrm{av}} = \frac{1}{N} \sum_{i=1}^{N} r_i, \tag{16}$$

where $r_{p,\mathrm{av}}$ is the average pore radius, N is the number of accessible voxels that wrap the pore region, and r_i is the distance from the pore center to the ith accessible voxels (solid or void voxels) that wrap the pore region. The probability density functions (PDFs) of the average radii of the pore bodies and of the pore throats are shown in Fig. 12. The average radii of pore bodies and pore throats are in the ranges of 2.7–7.3 and 1.3–6.9 μm, respectively. 79.2% of the pore bodies have average radii in the range of 4.3–5.7 μm. 72.5% of the pore throats have average radii in the range of 2.1–3.3 μm.

The average pore radius cannot elucidate the variation or dispersion of the distances from the pore center voxel to the accessible voxels that wrap the pore region. Such variation, to some extent, reflects the topology of the pore. To illustrate this variation, the population standard deviation of the average pore radius is determined:

$$\mathrm{SD}_{\mathrm{rp}} = \sqrt{\frac{1}{N} \sum_{i=1}^{N} (r_i - r_{p,\mathrm{av}})^2}. \tag{17}$$
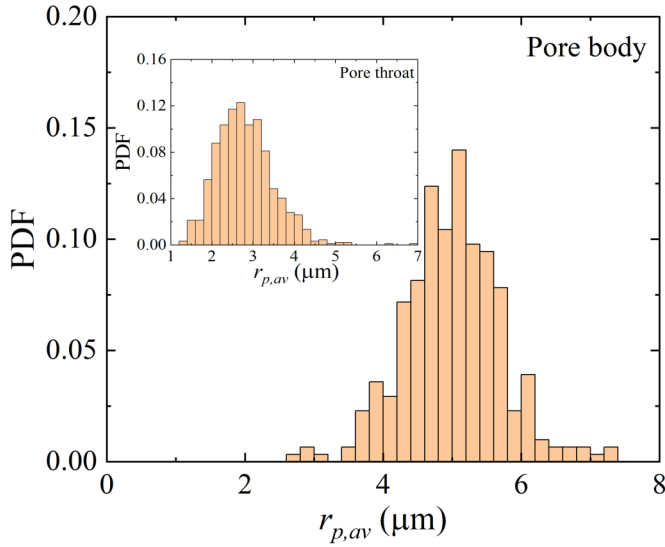
FIG. 12. Probability density functions (PDFs) of the average radii of the pore bodies and of the pore throats.

The PDFs of SD_{rp} for the pore bodies and the pore throats are presented in Fig. 13. For the pore bodies, SD_{rp} is from 0.75 to 3.15 μm, and 79.2% of SD_{rp} is in the range 1.25–1.95 μm. For the pore throats, SD_{rp} is from 0.25 to 3.55 μm, and 76.9% of SD_{rp} is in the range 0.55–1.25 μm.

To further elucidate the pore anisotropy, we show in Fig. 14 the PDFs of $r_{p,\max}/r_{p,\min}$ for the pore bodies and the pore throats. Here, $r_{p,\max}$ and $r_{p,\min}$ are the largest and smallest distances from the pore center voxel to the accessible voxels that wrap the pore region, respectively. Thus, $r_{p,\max}/r_{p,\min}$, to some extent, characterizes the aspect ratio of the pore. For the pore bodies,
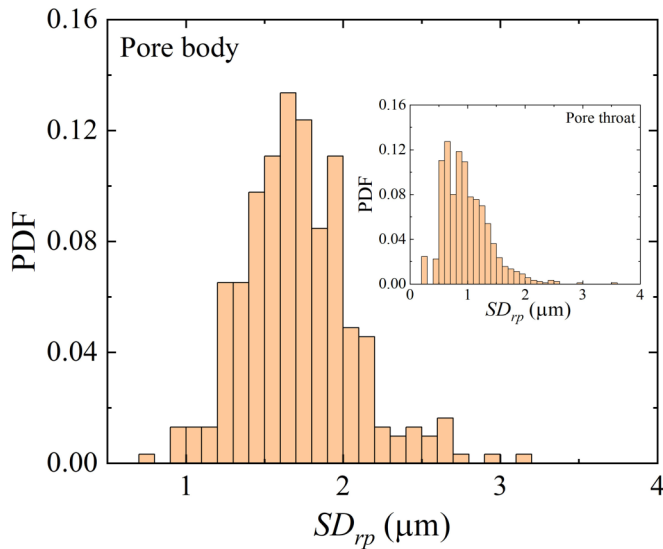

FIG. 13. PDFs of SD_{rp} for the pore bodies and the pore throats. SD_{rp} is the population standard deviation of the average pore radius.
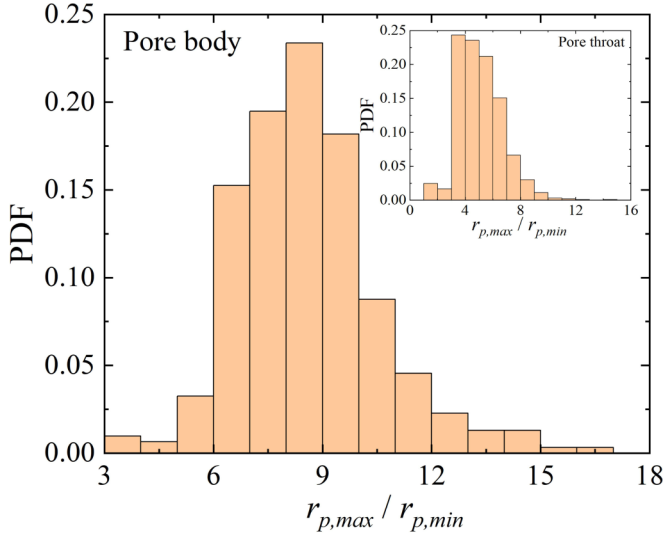
FIG. 14. PDFs of $r_{p,\max}/r_{p,\min}$ for the pore bodies and the pore throats. $r_{p,\max}$ and $r_{p,\min}$ are the largest and smallest distances from the pore center voxel to the accessible voxels that wrap the pore region, respectively.

$r_{p,\max}/r_{p,\min}$ ranges from 3.5 to 16.5, and 76.3% of $r_{p,\max}/r_{p,\min}$ is located in the range 6.5–9.5. For the pore throats, $r_{p,\max}/r_{p,\min}$ ranges from 1.5 to 14.5, and 84.2% of $r_{p,\max}/r_{p,\min}$ is located in the range 3.5–6.5. The results in Fig. 14 show clearly that the pore radii can be quite different in various directions.

The variations of the pore surface area, A_s, against the pore volume, V_p, for the pore bodies and pore throats are shown in Fig. 15. Here, the pore surface area is the sum of the areas of the interfaces between the void voxels and the solid boundary voxels that wrap the pore region. We find that the
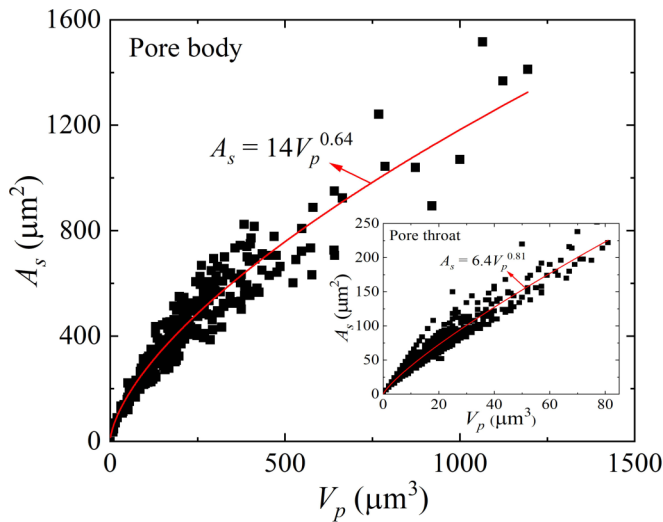

FIG. 15. Variations of A_s with V_p for the pore bodies and the pore throats. A_s is the pore surface area, and V_p is the pore volume.
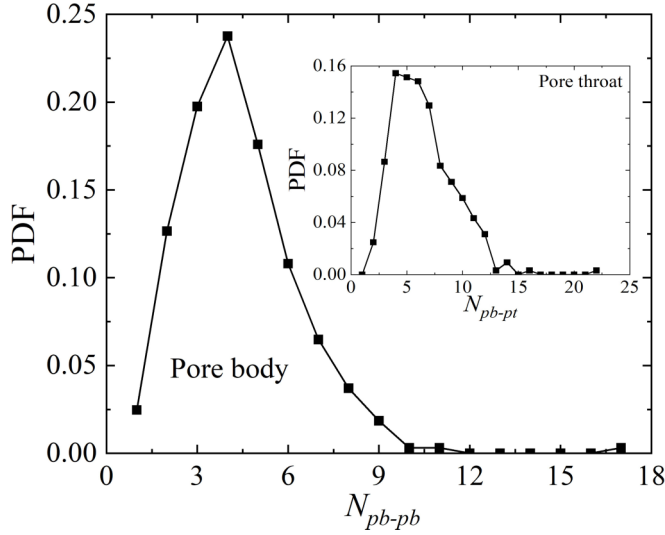
FIG. 16. PDFs of $N_{\text{pb-pb}}$ and $N_{\text{pb-pt}}$. $N_{\text{pb-pb}}$ is the number of pore bodies connected to a pore body by the medial axis. $N_{\text{pb-pt}}$ is the number of pore throats connected to a pore body.

pore surface area is a power-law function of the pore volume. For the pore bodies, $A_S = 14V_p^{0.64}$. For the pore throats, $A_S = 6.4V_p^{0.81}$.

The PDF of the coordination number is presented in Fig. 16. The coordination number depicts the pore connectivity. Since two pore bodies can be connected by more than one pore throat, two types of coordination numbers are employed. The first is the number of pore bodies connected to a pore body through the medial axis, $N_{\text{pb-pb}}$. The second is the number of pore throats connected to a pore body, $N_{\text{pb-pt}}$. As shown in Fig. 16, $N_{\text{pb-pb}}$ is in the range 1–11, and $N_{\text{pb-pt}}$ ranges from 1 to 25. The distribution range of $N_{\text{pb-pt}}$ is larger than that of $N_{\text{pb-pb}}$. This indicates that two pore bodies can be connected by more than one pore throat [e.g., see Fig. 11(b)]. If two pore bodies are connected by just only one pore throat, then the distribution ranges of $N_{\text{pb-pb}}$ and $N_{\text{pb-pt}}$ should be the same. Hence, there are two types of pore throats. The pore throat of type A is the only path between two pore bodies. The pore throat of type B is one of the paths between two pore bodies. These two types of pore throats are illustrated in Fig. S13 in the Supplemental Material [33].

B. Single-phase flow

To simulate the fluid flow in the pore network extracted from the 3D fibrous porous material shown in Fig. 10, it is necessary to know the flow conductivity between two nodes, which is determined by the following procedure:

(i) The absolute permeability of the fibrous porous material is calculated by using the direct numerical simulation (the lattice Boltzmann method is used; see Ref. [36] for more details) so as to validate the results obtained by the pore network model.

(ii) The cross section of the slice perpendicular to the medial axis is abstracted as a rectangular, triangular, or elliptical cross section (these will be called the virtual cross sections hereafter). Based on the perimeter and the cross-sectional area of the slice perpendicular to each void voxel at the medial axes, the flow conductivities of the virtual cross sections can be determined (see Appendix B) and are used for the realistic slices perpendicular to the medial axis. Based on the flow conductivity of each slice, the flow conductivity between two adjacent nodes is obtained by using Eq. (8).

TABLE II. Comparison of the absolute permeabilities in the x-, y-, and z-directions of the fibrous porous material shown in Fig. 10(b) determined by the direction of the numerical simulation and the pore network modeling.

	K_x (Darcy)	K_y (Darcy)	K_z (Darcy)
LBM	5.57	5.71	3.61
PNM (Rectangular cross section)	12.86	13.40	6.71
PNM (Triangular cross section)	8.28	7.90	4.98
PNM (Elliptical cross section)	14.16	17.08	10.39

(iii) The absolute permeability of the extracted pore network is determined and compared against the direct numerical simulation results so as to determine the shape of the virtual cross section. Table II shows the absolute permeabilities in the x-, y-, and z-directions of the fibrous porous material (Fig. 10) determined by direct numerical simulation and the pore network model. The magnitudes of the absolute permeability obtained from these two approaches are in the same order. According to the results presented in Table II, the triangle is superior to a rectangle or an ellipse, and hence it is used as the shape of the virtual cross section in the extracted pore network.

Here, the flow conductivity between two nodes in the extracted pore network is determined by the size and the shape of the virtual cross section. This method leads to fast calculation of the flow conductivity between two nodes, but it is not accurate enough. A more accurate method to obtain the flow conductivity between two nodes is to rely on direct numerical simulations, but they are computationally intensive. In future work, we shall combine direct numerical simulations, e.g., LBM, and the machine learning technique so as to obtain the flow conductivity between two nodes with high accuracy and reasonable computational resources, e.g., as in Ref. [17].

C. Quasistatic drainage

The quasistatic drainage of a nonwetting phase displacing a wetting phase in the extracted pore network from the 3D fibrous porous material shown in Fig. 10 is also simulated by using the algorithm depicted in Sec. VI. The contact angle taken in the wetting phase of the surface walls of the pore network is 0°. The corner films are not considered. The pore network is initially filled with a wetting phase. The inlet face of the extracted pore network is connected to a nonwetting reservoir, as illustrated by the blue surface in Fig. 17. In this figure, the nodes and the bonds invaded by the nonwetting phase at the various nonwetting phase saturations are presented. The spheres and the lines represent the nodes and bonds filled with the nonwetting phase, respectively. The solid matrix and the nodes and bonds occupied by the wetting phase are not shown for the sake of clarity.

For the quasistatic drainage in a porous material, the two-phase displacement is dominated by the threshold pressure of each pore. This indicates that the accuracy of the pore network model for the quasistatic drainage depends on the determination of the threshold pressure of each node if the extracted pore network is accurate. The method to determine the threshold pressures of the nodes in the extracted pore network is detailed and validated in Sec. VI. Thus, we believe that the pore network modeling of the quasistatic drainage process in the fibrous porous material shown in Fig. 17 is reasonable, even though it is not compared directly against the experimental results.

Although challenging, a comparison of the pore network modeling results on the two-phase transport in real 3D porous media against the experimental data is of vital importance, especially for the transport processes controlled not only by the threshold pressure of each pore but also by the mass transfer, e.g., evaporation in porous media. For evaporation in porous media, the liquid in the corners of pores, i.e., the so-called corner films, can play an important role [37–39]. Hence, the corners of pores should be taken into account in the extracted pore networks. Extraction of the pore networks with pore corners from realistic porous media is envisioned as a future extension of the present study.
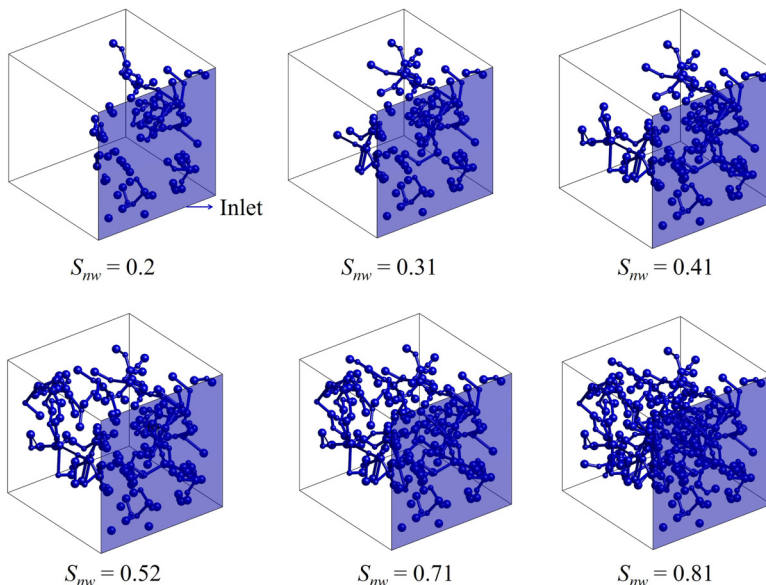
FIG. 17. Pore network modeling the quasistatic drainage process in the 3D fibrous porous media shown in Fig. 10(b). The nonwetting phase occupied nodes and bonds are shown in blue. S_{nw} is the saturation of the nonwetting phase.

VIII. CONCLUSIONS

In the present study, we propose a method to extract the medial axis from porous media with pores of high aspect ratios based on the concept of the omnidirectional Euclidean distance (OED). In our pore network extraction method, the medial axis of the void space is first determined, followed by the centers and regions of pore bodies and pore throats. Such an extraction method preserves the topological and morphological properties of the void spaces in porous media. To account for the case in which two pore bodies can be connected by more than one pore throat, the extracted pore networks are defined to be composed of nodes and bonds. The centers of nodes are the centers of pore bodies or pore throats, resulting in two types of nodes, namely pore body nodes and pore throat nodes. The bonds between two nodes depict the connection between pore bodies and pore throats. The proposed pore network extraction method is robust and is insensitive to the noise of the voxelized porous media.

Based on the proposed method, we successfully extract the pore network of a quasi-2D microfluidic porous material with pores of the same height. The medial axis determined based on the OED is superior to that based on the traditional Euclidean distance. The pore network modeling results regarding the single-phase flow and the quasistatic drainage in the quasi-2D microfluidic porous material are in good agreement with the direct numerical simulation results and/or the experimental data, further demonstrating the effectiveness of our proposed method. To further show the feasibility of the pore network extraction method proposed in the present study, we also extract the pore network from a 3D fibrous porous material, and we perform pore network modeling of the single-phase and the quasistatic drainage in this 3D fibrous porous material.

In the present study, a deterministic approach is employed to segment the pore body and the pore throat regions in the voxelized porous media. This approach is based on the distance of each void voxel to the medial axis. The proposed segmentation approach contributes to a detailed study of the properties of the void spaces in porous media, especially for porous materials with pores of high aspect ratios. To suitably disclose the properties of the pore structures, the porous media need to be voxelized with a high resolution so that each pore region contains at least more than one voxel.

The proposed pore network extraction method provides an effective tool not only for characterizing the structural properties of void space in porous media with pores of high aspect ratios, but also for modeling the multiphase transport in porous media. However, more future studies are needed so as to improve the extraction efficiency and to include the pore corners in the extracted pore networks.

ACKNOWLEDGMENTS

APPENDIX A: INFLUENCE OF IMAGE NOISE ON THE MEDIAL AXIS EXTRACTION

To extract the pore network from a realistic porous material, the void structure of this porous material should be obtained first, e.g., by using the micro-CT technique. However, the image noise is inevitable during acquisition of the void structures of realistic porous media. Such image noise can affect the extracted medial axis.

To check if the image noise influences the medial axis extracted based on the proposed ODOHT algorithm, we compare in Fig. 18 the extracted medial axes for the void structures with and without the image noise. The red voxels are those at the medial axis. Both the convex surface noise and the concave surface noise are considered. The convex surface noise generates additional void voxels, Fig. 18(b). The concave surface noise transfers the void voxels to the solid ones, Fig. 18(c). As shown in Fig. 18, the extracted medial axis is not affected by the image noise. That is to say, the ODOHT algorithm proposed in the present study is insensitive to image noise. The reason could be as follows.

In the ODOHT algorithm, the hierarchy of the void voxel can be clearly distinguished. The hierarchical levels of the void voxels are numbered in Fig. 18. The void voxels have different hierarchical levels. The void voxel generated because of the convex surface noise is surrounded
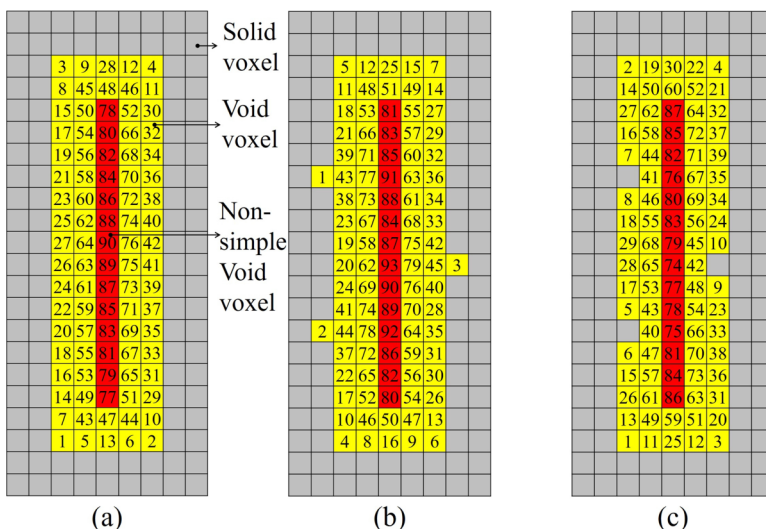

FIG. 18. Medial axis extracted from the void space with and without noise. (a) Without noise, (b) with convex surface noise, and (c) with concave surface noise. The numbers represent the hierarchical levels of the void voxels. The void voxels at the medial axis are shown in red.

by solid voxels, and hence it has a lower OED and a lower hierarchical level; see Fig. 18(b). The hierarchical levels of the three void voxels generated because of the convex surface noise shown in Fig. 18(b) are 1, 2, and 3, respectively. Thus, the void voxels generated because of the convex surface noise will be scanned and checked first to see if they are the simple void voxel in the ODOHT algorithm. Since these void voxels are surrounded by solid voxels, Eqs. (1)–(3) are applicable to these void voxels. As a result, the void voxels generated because of the convex surface noise will be identified as simple void voxels.

Both the convex and concave surface noise affect the hierarchical levels of the void voxels, as shown in Fig. 18. But, for the hierarchical levels of the void voxels determined based on the OED, the void voxels near the medial axis have larger OEDs than those away from the medial axis. In this regard, the image noise cannot change the trend of the scanning order in the ODOHT algorithm, i.e., from the void voxels away from the medial axis to those near the medial axis. As a result, the medial axis determined by the ODOHT algorithm is not affected by the image noise, Fig. 18.

APPENDIX B: DETERMINATION OF THE FLOW CONDUCTIVITY OF THE SLICE PERPENDICULAR TO THE MEDIA AXIS BY THE VIRTUAL CROSS SECTION

The flow conductivity of the virtual cross section of the slice perpendicular to the medial axis is determined based on the perimeter and cross-sectional area of the slice.

The flow conductivity of the slice (e.g., the mth slice) with a virtual rectangular cross section is determined by Eqs. (9)–(11). The width and height of the virtual rectangular cross section, $w_{v,s,m}$ and $h_{v,s,m}$, are determined as

$$w_{v,s,m}h_{v,s,m} = A_{s,m}, \quad 2(w_{v,s,m} + h_{v,s,m}) = C_{s,m}, \tag{B1}$$

where $A_{s,m}$ and $C_{s,m}$ are the cross-sectional area and perimeter of the mth slice, respectively.

The flow conductivity of the slice (e.g., the mth slice) with a virtual triangular cross section is determined as

$$g_{s,m} = \frac{l_{s,m}A_{s,m}^2}{\alpha_{s,m}}, \tag{B2}$$

for which $l_{s,m}$ is the length of the mth slice, $A_{s,m}$ is the cross-sectional area of the mth slice, and $\alpha_{s,m}$ is the dimensionless geometrical correction factor. As in Ref. [40], $\alpha_{s,m}$ for the triangular cross section is

$$\alpha_{s,m} = \frac{25}{17G_{s,m}} + \frac{40\sqrt{3}}{17}, \tag{B3}$$

where $G_{s,m}$ is the dimensionless shape factor of the mth slice and is equal to

$$G_{s,m} = \frac{A_{s,m}}{P_{s,m}^2}, \tag{B4}$$

where $P_{s,m}$ is the perimeter of the mth slice.

The flow conductivity of the slice (e.g., the mth slice) with a virtual ellipse cross section is also determined by Eq. (B2). In this case, the dimensionless geometrical correction factor, $\alpha_{s,m}$, is determined as

$$\alpha_{s,m} = \frac{8}{3G_{s,m}} - \frac{8\pi}{3}. \tag{B5}$$

Here, $G_{s,m}$ is calculated by Eq. (B4).

[1] Q. Xiong, T. G. Baychev, and A. P. Jivkov, Review of pore network modelling of porous media: Experimental characterisations, network constructions and applications to reactive transport, J. Contam. Hydrol. **192**, 101 (2016).

[2] A. Raoof, H. M. Nick, S. M. Hassanizadeh, and C. J. Spiers, PoreFlow: A complex pore-network model for simulation of reactive transport in variably saturated porous media, Comput. Geosci. **61**, 160 (2013).

[3] J. Ghassemzadeh, M. Hashemi, L. Sartor, and M. Sahimi, Pore network simulation of imbibition into paper during coating: I. Model development, AIChE J. **47**, 519 (2001).

[4] J. Ghassemzadeh and M. Sahimi, Pore network simulation of fluid imbibition into paper during coating: II. Characterization of paper's morphology and computation of its effective permeability tensor, Chem. Eng. Sci. **59**, 2265 (2004).

[5] V. Joekar-Niasar and S. M. Hassanizadeh, Specific interfacial area: The missing state variable in two-phase flow equations? Water Resour. Res. **47**, W05513 (2011).

[6] A. Aghaei and M. Piri, Direct pore-to-core up-scaling of displacement processes: Dynamic pore network modeling and experimentation, J. Hydrol. **522**, 488 (2015).

[7] D. B. Silin, G. Jin, and T. W. Patzek, Robust determination of the pore-space morphology in sedimentary rocks, in *SPE Annual Technical Conference and Exhibition* (OnePetro, 2003).

[8] D. Silin and T. Patzek, Pore space morphology analysis using maximal inscribed spheres, Physica A **371**, 336 (2006).

[9] A. S. Al-Kharusi and M. J. Blunt, Network extraction from sandstone and carbonate pore space images, J. Pet. Sci. Eng. **56**, 219 (2007).

[10] H. Dong and M. J. Blunt, Pore-network extraction from micro-computerized-tomography images, Phys. Rev. E **80**, 036307 (2009).

[11] F. Arand and J. Hesser, Accurate and efficient maximal ball algorithm for pore network extraction, Comput. Geosci. **101**, 28 (2017).

[12] A. Q. Raeini, B. Bijeljic, and M. J. Blunt, Generalized network modeling: Network extraction as a coarse-scale discretization of the void space of porous media, Phys. Rev. E **96**, 013312 (2017).

[13] T. G. Baychev, A. P. Jivkov, A. Rabbani, A. Q. Raeini, Q. Xiong, T. Lowe, and P. J. Withers, Reliability of algorithms interpreting topological and geometric properties of porous media for pore network modeling, Transp. Porous Media **128**, 271 (2019).

[14] A. Rabbani, S. Jamshidi, and S. Salehi, An automated simple algorithm for realistic pore network extraction from micro-tomography images, J. Pet. Sci. Eng. **123**, 164 (2014).

[15] T. Agaesse, A. Lamibrac, F. N. Buchi, J. Pauchet, and M. Prat, Validation of pore network simulations of ex-situ water distributions in a gas diffusion layer of proton exchange membrane fuel cells with X-ray tomographic images, J. Power Sources **331**, 462 (2016).

[16] J. T. Gostick, Versatile and efficient pore network extraction method using marker-based watershed segmentation, Phys. Rev. E **96**, 023307 (2017).

[17] A. Rabbani and M. Babaei, Hybrid pore-network and lattice-Boltzmann permeability modeling accelerated by machine learning, Adv. Water Res. **126**, 116 (2019).

[18] A. Rabbani, P. Mostaghimi, and R. T. Armstrong, Pore network extraction using geometrical domain decomposition, Adv. Water Res. **123**, 70 (2019).

[19] Z. A. Khan, A. Elkamel, and J. T. Gostick, Efficient extraction of pore networks from massive tomograms via geometric domain decomposition, Adv. Water Res. **145**, 103734 (2020).

[20] T. Lee and R. L. Kashyap, Building skeleton models via 3D medial surface/axis thinning algorithms, CVGIP: Graph. Models Image Proc. **56**, 462 (1994).

[21] W. B. Lindquist and A. Venkatarangan, Investigation 3D geometry of porous media from high resolution images, Phys. Chem. Earth Part A **24**, 593 (1999).

[22] R. Al-Raoush, K. Thompson, and C. S. Willson, Comparison of network generation techniques for unconsolidated porous media, Soil Sci. Soc. Am. J. **67**, 1687 (2003).

[23] R. I. Al-Raoush and C. S. Willson, Extraction of physically realistic pore network properties from three-dimensional synchrotron X-ray microtomography images of unconsolidated porous media systems, J. Hydrol. **300**, 44 (2005).

[24] Z. Jiang, K. Wu, G. Couples, M. I. J. van Dijke, K. S. Sorbie, and J. Ma, Efficient extraction of networks from three-dimensional porous media, Water Resour. Res. **43**, W12S03 (2007).

[25] Z. Jiang, M. I. J. van Dijke, S. Geiger, J. Ma, G. D. Couples, and X. Li, Pore network extraction for fractured porous media, Adv. Water Res. **107**, 280 (2017).

[26] A. Q. Raeini, B. Bijeljic, and M. J. Blunt, Generalized network modeling of capillary-dominated two-phase flow, Phys. Rev. E **97**, 023308 (2018).

[27] A. Q. Raeini, J. Yang, I. Bondino, T. Bultreys, M. J. Blunt, and B. Bijeljic, Validating the generalized pore network model using micro-CT images of two-phase flow, Transp. Porous Media **130**, 405 (2019).

[28] H. J. Vogel and K. Roth, Quantitative morphology and network representation of soil pore structure, Adv. Water Res. **24**, 233 (2001).

[29] J. T. Gostick, M. W. Fowler, M. A. Ioannidis, M. D. Pritzker, Y. M. Volfkovich, and A. Sakars, Capillary pressure and hydrophilic porosity in gas diffusion layers for polymer electrolyte fuel cells, J. Power Sources **156**, 375 (2006).

[30] K. M. Gerke, T. O. Sizonenko, M. V. Karsanina, E. V. Lavrukhin, V. V. Abashkin, and D. V. Korost, Improving watershed-based pore-network extraction method using maximum inscribed ball pore-body positioning, Adv. Water Res. **140**, 103576 (2020).

[31] Z. Yi, M. Lin, W. Jiang, Z. Zhang, H. Li, and J. Gao, Pore network extraction from pore space images of various porous media systems, Water Resour. Res. **53**, 3424 (2017).

[32] D. G. Morgenthaler, Three-dimensional simple points: Serial erosion, parallel thinning, and skeletonization, Tech. Rep. TR-1005 (Comput. Vision Lab., Comput. Sci. Cent., Univ. of Maryland, College Park, 1981).

[33] See Supplemental Material at http://link.aps.org/supplemental/10.1103/PhysRevFluids.7.014304 for more details on pore network extraction.

[34] M. A. Tirunarayanan and A. Ramachandran, Correlation of isothermal pressure drop in rectangular ducts, in *Proceedings of Australasion Conference on Hydraulic Fluid Mechanics* (University of Auckland, 1965), p. A213.

[35] R. Wu, A. Kharaghani, and E. Tsotsas, Two-phase flow with capillary valve effect in porous media, Chem. Eng. Sci. **139**, 241 (2016).

[36] C. Manwart, U. Aaltosalmi, A. Koponen, R. Hilfer, and J. Timonen, Lattice-Boltzmann and finite-difference simulations for the permeability for three-dimensional porous media, Phys. Rev. E **66**, 016702 (2002).

[37] R. Wu, T. Zhang, C. Ye, C. Y. Zhao, E. Tsotsas, and A. Kharaghani, Pore network model of evaporation in porous media with continuous and discontinuous corner films, Phys. Rev. Fluids **5**, 014307 (2020).

[38] N. Vorhauer, Y. J. Wang, A. Kharaghani, E. Tsotsas, and M. Prat, Drying with formation of capillary rings in a model porous medium, Transp. Porous Media **110**, 197 (2015).

[39] A. Kharaghani, H. T. Mahmood, Y. J. Wang, and E. Tsotsas, Three-dimensional visualization and modeling of capillary liquid rings observed during drying of dense particle packings, Int. J. Heat Mass Transf. **177**, 121505 (2021).

[40] N. A. Mortensen, F. Okkels, and H. Bruus, Reexamination of Hagen-Poiseuille flow: Shape dependence of the hydraulic resistance in microchannels, Phys. Rev. E **71**, 057301 (2005).